Geochronological constraints on post-collisional shear belt in the Variscides of Sardinia, Italy

GEOCHRONOLOGICAL CONSTRAINTS ON POST-COLLISIONAL 1 SHEAR ZONES IN THE VARISCIDES OF SARDINIA (ITALY)

R. Carosi[1], C. Montomoli[1], M. Tiepolo[2], and C. Frassi[1]

1 Dipartimento di Scienze della Terra, Università di Pisa, via S. Maria, 53, 56126, Pisa, Italy;
2 IGG, CNR Istituto di Geoscienze e Georisorse, Unità di Pavia, Via Ferrata, 1, 27100, Pavia, Italy.

TERRA NOVA

Vol 24, p. 42–51, 2012

doi: 10.1111/j.1365-3121.2011.01035.x

(Postprint article)

Geochronological constraints on post-collisional shear zones in the Variscides of Sardinia (Italy)

R. Carosi[1], C. Montomoli[1], M. Tiepolo[2], and C. Frassi[1]

[1] *Dipartimento di Scienze della Terra, Università di Pisa, via S. Maria, 53, 56126, Pisa, Italy;* [2] *IGG, CNR Istituto di Geoscienze e Georisorse, Unità di Pavia, Via Ferrata, 1, 27100, Pavia, Italy.*

ABSTRACT

The post-collisional tectonics in the inner zone of the Variscan belt of Corsica-Sardinia recorded a dextral transpression developed with an orogen-parallel tectonic transport. Recent works documented the presence of nearly parallel dextral and sinistral crustal-scale shear zones responsible of the exhumation of the metamorphic complexes. To constrain, for the first time, the timing of both shear zones and the timing of the transpressional shearing, zircons and monazites were collected for U-Th-Pb ages. Results indicate that the shear zones have been active at *c.* 320 Ma in a transpressional setting, widespread in the Southern European Variscan belt.

Introduction

Shear zones represent efficient ways to exhume deep-seated rocks in collisional orogens (Passchier and Coehlo, 2006), transpressional belts (Goscombe and Gray, 2009) and extensional settings. As consequences, assessing the geometry and kinematics of mylonitic belts provide informations to individuate the mechanisms of exhumation (Xypolias and Koukouvelas, 2001; Law *et al.*, 2004; Carosi *et al.*, 2006; Larson and Godin, 2009) whereas the timing of shear activity constraints the tectono-metamorphic evolution of the exhumed rocks.

Sardinia island offers a continuous transect across the Southern Variscan belt from the external areas (to the south) up to the inner zone (to the north) (Carmignani *et al.*, 1994) (Fig. 1). After the D1 collisional phase the inner zone was affected by an E-W striking D2 dextral transpression (Carosi and Palmeri, 2002, Carosi and Oggiano, 2002), running for more than

150 km, close to the boundary between the Medium Grade Metamorphic Complex (MGMC) (amphibolite-facies metasedimentary and metavolcanic rocks), to the south, and the High Grade Metamorphic Complex (HGMC) (migmatites) to the north (Fig. 1). D2 transpressional shear zones contributed to the exhumation of both metamorphic complexes (Carosi *et al.*, 2004, 2005; Iacopini *et al.*, 2008).

Despite the timing of metamorphic evolution of HGMC has been constrained by U-Pb geochronology (Giacomini *et al.*, 2005, 2006), the timing of the tectonic events is poorly defined. Di Vincenzo *et al.* (2004) constrained dextral shearing in the MGMC at nearly 320-315 Ma (Ar-Ar on white mica).

The aim of this paper is to constrain the age of D2 dextral and sinistral shear zones by U-Th-Pb isotopic measurements on both monazite and zircon.

Shear belts in the inner zone

The Variscan belt in Sardinia developed from deformation and metamorphism of the northern margin of Gondwana during the Carboniferous, involving sedimentary and magmatic sequences, ranging from Cambrian to Lower Carboniferous, tectonically transported from NE to SW (Carmignani *et al.*, 1994). The belt is characterized by a prograde Barrovian metamorphism increasing from SW to NE. Between the HGMC and MGMC a D2 shear belt has been recognized and for nearly 20 years it has been regarded as affected by only dextral shearing (Carmignani *et al.*, 1994).

Recently Carosi *et al.* (2009) documented within the D2 shear belt:

(1) a sinistral ductile top-to-the NW shear zone (Figs. 2 and 3) characterized by mylonites;

(2) a dextral ductile to brittle-ductile top-to-the SE shear zone (Figs. 2 and 4a-b) associated to mylonites and later phyllonites. The phyllonites developed at the boundary between the two metamorphic complexes (Fig. 4).

D2 sinistral shear zone developed within fine-grained gneisses, sillimanite - bearing migmatites, pegmatites and alm + pl + ky ± sil micaschists and gneisses (HGMC) (Fig. 2) whereas D2 dextral shear zone developed within grt+pl ± ky± st - bearing metasedimentary sequences (MGMC) (Fig. 2) and in fine-grained gneisses (HGMC). Dextral and sinistral mylonites overprint prograde Barrovian index minerals (grt, pl, st and ky) grown during the

D1 collisional stage (Ricci *et al.*, 2004) whereas sillimanite grew parallel or oblique to the D2 sinistral shear planes in a decompressive path (Carosi *et al.*, 2009).

The occurrence of dextral phyllonite around lenses containing sinistral mylonites constrains that its dextral shearing postdates the sinistral shearing event. A network of dextrally sheared cataclasites overprint both phyllonites and sinistral shear zones. According to structural relations, the sinistral shear started earlier, whereas the dextral shear event developed later and remained dominant until the rocks reached upper crustal levels (Fig. 2).

Deformation within both sinistral and dextral shear zones involved non-coaxial flow with a contemporaneous contribution of pure and simple shear (Frassi *et al.*, 2009). Considering the km-scale length of shear zones, the dip-slip component is potentially important in the exhumation of the metamorphites. A rough estimate of the minimum vertical displacement, calculated using L2 lineation plunge (20-25°) and the length of shear zones, is around 4 km for sinistral and 1 km for the dextral shear zones. However, as dextral shear zones developed in northern Sardinia for more than 150 km, vertical displacement must be higher.

D2 microstructures, thermobarometry and P-T trajectories predicted a minimum exhumation of c. 10 km and c. 10-15 km respectively for the MGMC and HGMC (Carosi and Palmeri, 2002; Carosi *et al.*, 2009; Di Vincenzo *et al.*, 2004; Casini *et al*., 2010). Common feature of transpressional belts is that horizontal displacement is constrained by kinematics whereas vertical displacement mainly by thermobarometry (Goscombe and Gray, 2009).

U-Th-Pb geochronology

Two samples from dextral shear zone (TDx and GDx) and three samples from sinistral shear zone (BSx, GSx2 and GSx3) were selected for U-Th-Pb analyses (Table 1; Fig. 2).

U-Th-Pb geochronology was carried out on zircons and monazites, with excimer laser ablation (ELA)-ICP-MS using spot size of 20 μm (Table 2). Zircons and monazites were separated with conventional methods and selected by different morphology, colors and dimensions. Before undertaking analysis, zircons and monazite structures were investigated by cathodoluminescence (CL) and backscattered electrons (BSE), respectively.

D2 sinistral mylonites

Zircons

Zircons from sinistral mylonites have a prismatic habitus and inherited cores surrounded by multiple overgrowths (Fig. 5a). Relicts of igneous textures such as oscillatory zoning characterize most of the domains. Occasionally the most inner cores display a rounded shape that can be related either to sedimentary transport or magmatic resorption (Vavra *et al.*, 1999).

Samples GSx3 and GSx2 give U-Pb Carboniferous ages yelding a mean Concordia age at 318 ± 5 Ma (Fig. 6a).

Some inherited cores with rounded shape reveal Proterozoic ages from 716 up to 2450 Ma (Appendix 2). Overgrowths with oscillatory zoning show a large and poorly defined cluster in the Proterozoic (between 550 and 650 Ma) and two well defined major clusters at 436±10 and 480±8 Ma (Fig. 6a). Noticeably some Lower Carboniferous age at 354±14 Ma and 330±14 Ma were found, corresponding to a metamorphic recrystallisation over an original magmatic texture (Fig. 5a).

Zircons from sample BSx show a major cluster at 460 Ma. Inherited cores with evidence of resorption yield older ages from *c.* 512 up to 620 Ma. No Carboniferous ages were found (Appendix 2).

Monazite

Monazite crystals show euhedral habitus. BSE images reveal the presence of multiple domains that are either continuous rims around a darker core or minor patches scattered within the crystal. Only few homogeneous grains were observed. Monazites from samples GSx2 and GSx3 show lesser-marked zoning than monazites from sample BSx. Monazites from sample GSx2 do not show the occurrence of multiple age domains. Eleven of the fifteen analyses yield U-Pb concordant results with a mean age of 325±4 Ma (2s; MSWD=1.4) that is statistically equivalent to the mean $^{208}Pb/^{232}Th$ age of 320±2 Ma (2s; MSWD=0.7) obtained from the same data set.

Results on monazite from sample GSx3 closely resemble those from sample GSx2 (Fig.6b). Nine of the twelve analyses yield U-Pb concordant ages with a mean value of 326±4 Ma (2s; MSWD=0.98). The mean $^{208}Pb/^{232}Th$ age from the same data set is slightly younger (316±5 Ma 2s; MSWD=3.5) but still consistent with the U-Pb age. No evidence of multiple age domains was observed.

23 analyses out of forty analyses from sample BSx gave U-Pb concordant results. Data define two major U-Pb age peaks at 321±8.0 Ma (2s; 8 analyses; MSWD=3.4) and 453±7.8 Ma (2s; 12 analyses; MSWD=2.6) (Fig. 6b, Appendix 3). A minor peak at 389±11 Ma (2s; 2

analyses) and a single U-Pb concordant age at 502±19 Ma (2s) were also observed. $^{208}Pb/^{232}Th$ ages are generally within error with U-Pb results. The analyses carried out on the bright outer domains give ages in the 321±8.0 Ma cluster in agreement with the results obtained on the GSx2 and GSx3 samples. The older ages were obtained in the inner cores and on the darker zones and are probably inherited domains.

D2 dextral mylonites

Zircons

Zircons from sample GDx have inherited cores and multiple overgrowths. Inner cores have round shape and no clear internal structure. Most of the overgrowths display a clear oscillatory zoning of magmatic origin. From zircon H1 a succession of event can be defined (Fig. 5b; Table 3). The inner core with an age of 531±16 Ma is overgrown by a first domain with oscillatory zoning at 482±17 Ma and by a second domain at 442±13 Ma. The same ages are found in other zircon crystals. An older age at 691±17 Ma and a significantly younger age (299±10 Ma) obtained at the outermost rim of crystal H4 (Fig. 5b; Table 3), were also found. Half of the age determinations from zircons in samples TDx yield concordant Proterozoic ages spanning from 597±17 to 1016±21 Ma (Appendix 2).

Monazites

Monazites from the dextral mylonites are generally smaller than those from the sinistral mylonites. BSE images do not reveal the presence of clear distinct domains or inheritance. Monazite crystals are generally homogeneous or patchy with irregular and lobate grain boundaries. Quartz inclusions are frequently observed (Fig. 7b).

In sample GDx only two of the 23 analyses yield U-Pb concordant results with a mean of 324±6.5 Ma (2s) that overlap the $^{208}Pb/^{232}Th$ age of 328±6 Ma (Fig. 8b). Few U-Pb discordant data give relatively young $^{206}Pb/^{238}U$ and $^{208}Pb/^{232}Th$ ages spanning from 278 to 207 Ma. They most likely track late stage alteration processes that has partially reset the U-Th-Pb system.

In sample TDx, 11 of the 29 analyses yield U-Pb concordant ages with a mean value of 321±4 Ma (2s; MSWD=0.95). The $^{208}Pb/^{232}Th$ mean age at 319 ±3.3 Ma (2s; MSWD =0.44) is in good agreement with the U-Pb results.

Discussion

Carosi *et al.* (2009) documented the presence of a sinistral shearing along the boundary between MGMC and HGMC. The superposition relationships indicate that sinistral shear zones started earlier than the dextral ones during the D2 transpressional event causing the early exhumation of the HGMC (Frassi *et al.*, 2009). However, U-Th-Pb geochronology with associated analytical errors do not allow to clearly separate sinistral and dextral shear events. This could be indicative of an initial activation of the sinistral shear belt and a shortafter switch to a dextral shearing. Ar/Ar data on dextral mylonites in northeastern Sardinia (Di Vincenzo *et al.*, 2004) give younger ages (320-315 Ma) and in addition to this dextral brittle/ductile mylonites overprint both sinistral and dextral shear zones. The occurrence of granitoids (e.g. Badesi granodiorite) emplaced at c. 300 Ma during the latest stages of dextral shearing (Oggiano *et al.,* 2007) allow to infer that dextral shear belt was active for a longer time with respect to the sinistral one.

The presence in dextral mylonites of relatively small monazite grains with irregular and lobate grain boundaries and homogeneous or patchy compositional domains (Fig. 7b) may be connected to successive dissolution/recrystallization events (Parrish, 1990; Bosse *et al.*, 2009 with references) related to fluid circulation. This may be confirmed by (1) the presence of younger ages until *c.* 260 Ma, (2) the presence of inclusions of quartz and the absence of inherited domains in monazite grains in dextral mylonites and (3) the partial resetting of monazite chronometers in the lenses of sinistral mylonites enveloped by dextral low-strain phyllonites. On the contrary, monazite from sinistral mylonites far from phyllonites (sample BSx) show straight boundaries and continuous rims with younger ages recorded close to rims and older ages recorded within the cores (Fig. 7a).

The new isotopic data presented above, lead to constrain at c. 320 Ma the switch from sinistral to the dextral shear (Frassi *et al.*, 2009). The dextral shear belt remained active for at least 15-20 Ma at upper structural levels partly matching the emplacement of the late Variscan batholith.

The activity of complex Variscan crustal-scale shear zones during exhumation of high-grade metamorphic rocks has been documented by Giacomini *et al.* (2008) in the granulites and amphibolites of southeast Corsica (Fig. 9). According to these authors sinistral shear zones at *c.* 320 Ma were active before the dominant dextral shear belt. In this frame, our

results suggest that at *c.* 320 Ma the low- and high-grade metamorphic complexes of Corsica-Sardinia block were affected by a network of sinistral and dextral shear belts causing exhumation by an overall transpressional deformation with an orogen-parallel tectonic transport. This could be caused by a change of orientation of the belt with respect to the regional stress field (Frassi *et al.*, 2009).

After an initial nearly orthogonal convergence the collisional belt evolved toward a transpressional-dominated deformation and orogen-parallel tectonic transport (Carosi and Palmeri, 2002, Carosi *et al.* 2005). The part of Gondwana margin from which Sardinian tectonic units were originated, was oriented with respect to the regional principal stress σ_1 in the right way to develop sinistral shearing. The switch to dextral shearing was caused by a relative rotation of the shear belt with respect to the regional principal stress σ_1 (Frassi *et al.*, 2009). This rotation could have been triggered by the developing oroclinal bends of the Variscan belt leading later to the Ibero-Armorican arc on the western part of the belt (Ribeiro *et al.,* 2007) and to another oroclinal bend on the eastern side (Fig. 10) (Corsini and Rolland, 2009).

The datation at ~ 320 Ma of the dextral shear belt in Sardinia confirms the proposed correlation with the dextral shear zones occurring in Corsica, Maures-Esterel and in the External Crystalline Massifs (ECM) connected to the regional East Variscan Shear Zone by Corsini and Rolland (2009) and Guillot and Ménot (2009) (Fig.10).

Zircons and monazites from sinistral mylonites show a major Ordovician cluster at 440-450 Ma, whereas older ages have been found only in the inherited core of zircons.

The data are in agreement with Giacomini *et al.* (2006) that suggest the presence of a late Ordovician magmatism active in the HGMC emplaced in an extensional back-arc setting. Similar model and ages have been reported in the ECM (Guillot and Menot, 2009) strengthening a common Paleozoic evolution for this part of the Variscan belt.

Moreover, in the last decades metamorphic core complexes have been indicated as responsible of the exhumation of deep seated rocks in the Variscides (e.g. Costa and Rey, 1995). Otherwise, in some localities of the Variscan belt such as Sardinia, Corsica (Giacomini *et al.*, 2008), NE Spain (Carreras, 2001; Druguet, 2001; Vilà *et al.*, 2007) Maures - Esterel massif (Corsini and Rolland, 2009) and External Crystalline Massifs (Guillot and Menot, 2009), transpression tectonics have been documented contributing to the exhumation of deep seated rocks at ~ 320 Ma.

Acknowledgments

Research supported by PRIN 2004 and Pisa University (R. Carosi and C. Montomoli). We thank G. Oggiano and two anonymous referees whose comments greatly improved the manuscript.

References

Bosse, V., Boulvais, V.P., Gautier, P., Tiepolo, M., Ruffet, G., Devidal, J.L., Cherneva, Z., Gerdjikov, I. and Paquette, J.L., 2009. Fluid-induced disturbance of the monazite Th-Pb chronometer: In situ dating and element mapping in pegmatites from the Rhodope (Greece, Bulgaria). *Chem. Geol.*, **261**, 286-302.

Carmignani, L., Carosi, R., Di Pisa, A., Gattiglio, M., Musumeci, G., Oggiano, G. and Pertusati, P. C., 1994. The Hercynian Chain in Sardinia (Italy). *Geod. Acta*, **7**, 31-47.

Carosi, R. and Oggiano, G., 2002. Structural evolution of North eastern Sardinia: insight on the tectonic evolution of the Variscan Belt. *C. R. Geosciences*, **334**, 287-294

Carosi, R. and Palmeri, R., 2002. Orogen parallel tectonic transport in the Variscan belt of northeastern Sardinia (Italy): implications for exhumation of medium-pressure metamorphic rocks. *Geol. Magazine*, **139**, 497-511.

Carosi, R., Di Pisa, A., Iacopini, D., Montomoli, C. and Oggiano, G., 2004. The structural evolution of the Asinara Island (NW Sardinia, Italy). *Geod. Acta*, **175**, 309-329.

Carosi, R., Frassi, C., Iacopini, D. and Montomoli, C., 2005. Post collisional transpressive tectonics in northern Sardinia (Italy). *J. V. Explorer*, **19** (3).

Carosi, R, Montomoli, C, Rubatto, D, Visonà, D., 2006**.** Normal-sense shear zones in the core of the Higher Himalayan Crystallines (Bhutan Himalaya): evidence for extrusion ? In *Channel Flow, Ductile Extrusion and Exhumation in Continental Collision Zones,* Law RD, Searle MP and Godin L (eds.). *Geol. Soc. London, Special Publications,* **268**, 425-444.

Carosi, R., Frassi, C. and Montomoli, C., 2009. Deformation during exhumation of medium- and high-grade metamorphic rocks in the Variscan chain in northern Sardinia (Italy). *Geol. J.*, **44**, 280-305.

Carreras, J., 2001. Zooming on Northern Cap de Creus shear zones. *J. Struct. Geol*., **23**, 1457-1486.

Casini, L., Funedda, A., Oggiano, G., 2010. A bilance foreland-hinterland deformation model for the Southern Variscan belt of Sardinia, Italy. Geol. J., **45**, 634-639.

Corsini, M. and Rolland, Y., 2009. Late evolution of the southern European Variscan belt: Exhumation of the lower crust in a context of oblique convergence. *Comptes Rendus Geosciences* 341, 214–223.

Costa, S. and Rey, P., 1995. Lower crustal rejuvenation and growth during post-thickening collapse: from a crustal section through a Variscan metamorphic core complex. *Geology* **23**, 905–8.

Di Vincenzo, G., Carosi, R. and Palmeri, R., 2004. The relationship between tectono-metamorphic evolution and argon isotope records in white mica: constraints from in situ 40Ar-39Ar laser analysis of the Variscan basement of Sardinia. *J. Petrol.*, **45**, 1013-1043.

Druguet, E., 2001. Development of high thermal gradients by coeval transpression and magmatism during the Variscan orogeny: insights from the Cap de Creus (Eastern Pyrenees), *Tectonophysics* **332**, 275-293.Ferrara, G., Ricci, C.A. and Rita, F. 1978. Isotopic ages and tectono-metamorphic history of the metamorphic basement of north-eastern Sardinia. *Contr. Min. Petrol.*, **68**, 99-106.

Frassi, C., Carosi, R., Montomoli, C. and Law, R.D., 2009. Kinematics and vorticity of flow associated with post-collisional oblique transpression in the Variscan Axial Zone of northern Sardinia (Italy). *J. Struct. Geol.*, **31**, 1458–1471.

Kretz, R., 1983. Symbols for rock-forming minerals. *Am. Miner*., **68**, 277-279.

Gasquet, D., Bertrand, J-M., Paquette, J-L., Lehmann, J., Ratzov, G., De Ascençâo Guedes, R., Tiepolo, M., Boullier A-M., Scaillet, S. and Nomade, S., 2010. Miocene to Messinian deformation and hydrothermal activity in a pre-Alpine basement massif of the French western Alps: new U-Th-Pb and argon ages from the Lauzière massif. Bull. Soc.géol. Fr., 181 (3), 227-241.

Giacomini, F., Bomparola, R.M. and Ghezzo, C., 2005. Petrology and geochronology of metabasites with eclogite facies relics from NE Sardinia: constraints for the Paleozoic evolution of Southern Europe. *Lithos*, **82**, 221-248.

Giacomini, F*.,* Bomparola, R.M., Ghezzo, C. and Guldbransen, H., 2006. The geodynamic evolution of the Southern European Variscides: constraints from the U-Pb geochronology and geochemistry of the lower Paleozoic magmatic-sedimentary sequences of Sardinia (Italy). *Contr. Min. Petrol.*, **152**, 19-42.

290 Giacomini, F., Dallai, L., Carminati, E., Tiepolo, M. and Ghezzo, C., 2008. Exhumation of a
291 Variscan orogenic complex: insights from the composite granulitic-amphibolitic
292 metamorphic basement of South-East Corsica (France). *J. Metam. Geol.*, **26**, 403-436.
293 Goscombe, B.D. and Gray, D.R., 2009. Metamorphic responses in orogens of different
294 obliquity, scale and geometry. *Gondwana Research*, **15**, 151-167.
295 Guillot, S., and Ménot, R.P., 2009. Paleozoic evolution of the Extern Crystalline Massifs of
296 the Western Alps. *C.R. Geosciences*, **341**, 253-265.
297 Horstwood, M.S.A., Foster, G.L., Parrish, R.R., Noble, S.R. and Nowell, G.M., 2003.
298 Common-Pb corrected in situ U-Pb accessory mineral geochronology by LA-ICP-MS.
299 *Journal Anal. At. Spectrom.*, **18**, 837-846.
300 Iacopini, D., Carosi, R., Montomoli, C. and Passchier, C.W., 2008. Strain analysis and
301 vorticity of flow in the Northern Sardinian Variscan Belt: recognition of a partitioned
302 oblique deformation event. *Tectonophysics*, **446**, 77-96.
303 Larson, K. and Godin, L., 2009. Kinematics of the Greater Himalayan sequence, Dhaulagiri
304 Himal: implications for the structural framework of central Nepal, *J. Geol. Soc. (Lond.)*,
305 **166**, 25–43. doi: 10.1144/0016-76492007-180.
306 Law, R.D., Searle, M.P. and Simpson, R.L., 2004. Strain, deformational temperatures and
307 vorticity of flow at the top of the Greater Himalayan Slab, Everest Massif, Tibet. *Journal*
308 *Geol. Soc. London*, **161**, 305-320.
309 Ludwig, K.R., 2003. ISOPLOT 3.00: A geochronological toolkit for Microsoft Excel
310 (Berkeley Geochronology Center, Berkely, California).
311 Oggiano, G., Casini, L., Rossi, P. and Mameli, P., 2007. Long lived dextral strike-slip
312 tectonics in the Southern Variscan Belt: evidences from two synkynematic intrusions of
313 North Sardinia (Italy). Abstract in: " Mechanics of Variscan Orogeny: a modern view on
314 orogenic research. A symposium dedicated to Philippe Matte. Géologie de la France, 2,
315 141.
316 Paquette, J.L. and Tiepolo, M., 2007. High resolution (5μm) U-Th-Pb isotope dating of
317 monazite with excimer laser ablation (ELA)-ICPMS. *Chem. Geol.*, **240**, 222-237.
318 Parrish, R., 1990. U-Pb dating of monazite and its application to geological problems. *Can. J.*
319 *Earth Sci.*, **27**,1431-1450.
320 Passchier, C. and Coelho, S., 2006. An outline of shear-sense analysis in high-grade rocks.
321 *Gondwana Research*, **10**, 66–76.

Ribeiro, A., Munhà, J., Dias, r., Mateus, A., Pereira, E., Ribeiro, L., Fonseca, P., Araùjo, A., Oliveira,T., Romão, J., Charminè, H., Coke, C. and Pedro, J., 2007. Geodynamic evolution of the SW Europe Variscides. *Tectonics*, **26**, TC6009, doi: 10.1029/2006TC002058.

Ricci, C.A., Carosi, R., Di Vincenzo, G., Franceschelli, M. and Palmeri, R., 2004. Unravelling the tectono-metamorphic evolution of medium-pressure rocks from collision to exhumation of the Variscan basement of NE Sardinia (Italy): a review. *Per. Mineral.*, **73**, 73-83.

Seydoux-Guillaume, A.M., Paquette, J.L., Wiedenbeck, M., Montel, J.M. and Heinrich, W., 2002. Experimental resetting of the U-Th-Pb system in monazite. *Chem. Geol.*, **191**, 165-181.

Tiepolo, M., 2003. In situ Pb geochronology of zircon with laser ablation - inductively coupled plasma - sector field mass spectrometry. *Chem. Geol.*, **199**, 159-177.

van Achterbergh, E., Ryan, C.G., Jackson, S.E. and Griffin, W., 2001. Data reduction software for LA-ICP-MS. In: *Laser ablation-ICPMS in the earth science* (P. Sylvester, ed.) Mineralogical Association of Canada, **29**, 239-243.

Vavra, G., Schmidt, R. and Gebauer, D., 1999. Internal morphology, habitat and U-Th-Pb microanalysis of amphibolite-to-granulite facies zircons: geochronology of Ivrea Zone (Southern Alps). *Contrib. Min. Petrol.*, **134**, 380-404.

Vilà, M., Pin C., Liesa M. and Enrique P., 2007. LP-HT metamorphism in a late orogenic transpressional setting, Albera Massif, NE Iberia: implications for the geodynamic evolution of the Variscan Pyrenees, J. *Metamorph. Geol.,* **25**, 321-347.

Wiedenbeck, M., Alle, P., Corfu, F., Griffin, W.L., Meier, M., Oberli, F., VonQuadt, A., Doddick, J.C. and Spiegel, W., 1995. Three natural zircon standards for U-Th-Pb, Lu-Hf, trace elements and REE analyses. *Geost. Newsletter*, **19**, 1-23.

Xypolias, P. and Koukouvelas, I.K., 2001. Kinematic vorticity and strain patterns associated with ductile extrusion in the Chermes shear zones (External Hellnides, Greece). *Tectonophysics* **338**, 59-77.

Figure captions

Fig. 1. Geological sketch map of northern Sardina and location of study area.

Fig. 2. (a) Geological sketch map of metamorphic complexes in south-western Gallura and location of samples used for U-Th-Pb isotopic measurements. Illustration includes orientation data (Schmidt diagram, lower hemisphere) of main structural elements (A2: F2 fold axes; S2: foliation; L2: object lineation; A3: F3 fold axes) from Medium Grade Metamorphic Complex and High Grade Metamorphic Complex. Sketched geological cross-section showing the appearance of Barrovian mineral (mineral abbreviation after Kretz, 1983) and the Medium and High Grade Metamorphic Complexes.

Fig. 3. Sinistral top-to-the NW shear zones and related orientation data (C': shear planes; S: mylonitic foliation; Lest: mineral lineation), representative of Samples GSx2-GSx3 (a) and representative of Sample BSx (b) respectively (1,5 cm coin for scale). (c)-(d) Photomicrographs of sinistral shear zones (plane polarized light). In (c) kyanite (Ky) is unstable and deformed by sinistral shearing (top-right corner) whereas sillimanite (Sil) grew parallel or oblique to S2 mylonitic foliation, constraints its growth during (or later) the decompressive path produced by the D2 oblique transpressive regime.

Fig. 4. Dextral top-to-the SE shear belt and related orientation data (C': shear planes; S: mylonitic foliation; Lest: mineral lineation). (a) D2 S-C and S-C' mylonitic fabrics from kyanite-bearing micaschists (five cent coins for scale). (b) Photomicrograph of S2 mylonitic foliation wrapped around deformed crystals of kyanite (Ky), staurolite (St) and plagioclase (Pl) (Bt: biotite, Ms: muscovite; Grt: garnet; plane polarized light). (c) Photomicrograph of phyllonites. Note the weak development of shear planes (C') at low angle respect to the mylonitic foliation. (d) Millimetric-thick cataclasites (grey dash lines).

Fig. 5. SEM-cathodoluminescence images of some zircon crystals separated from sinistral (a) and dextral (b) shear zones. Dimension and location of analytical spot and $^{206}Pb/^{238}U$ isotopic ages (2σ error) are also showed. Data from Appendix 2.

Fig. 6. U/Th/Pb isotopic data from sinistral top-to-the NW shear belt. (a) U/Pb concordia diagram and related histogram and density curve for zircons. Main Variscan events are also showed. (b) Th/Pb and U/Pb histograms and density curves for monazites.

Fig. 7. BSE images and rim-to-rim age traverses of some monazite crystals separated from sinistral (a) and dextral (b) shear belts. The location and the size of ICP-MS laser ablation spots and their corresponding Th/Pb/U ages (2σ error) are also showed. Data from Appendix 3.

Fig. 8. U/Th/Pb isotopic data from dextral top-to-the SE shear belt. (a) U/Pb concordia diagram and related histogram and density curve for zircons. (b) Th/Pb and U/Pb histograms and density curves for monazites.

Fig. 9. Sinistral (A) and dextral (B) steeply dipping shear zones, showing an orogen-parallel tectonic transport in the High Grade Metamorphic Complex of Southern Corsica, in Between Fautea and Solenzara, dated at ~ 320 Ma by Giacomini *et al.* (2008).

Fig. 10. Permian reconstruction of the Variscan belt of western Europe (modified after Guillot & Menot, 2009). The East Variscan shear zone affects the External Crystalline massifs and Corsica and Sardinia (Sa: Sardinia; Co: Corsica; arg: Argentera massif; Bell-ois: Belledonne-Ois. Ar-mbt: Mont Blanc; aar-go: Aar-Gottard massifs; SASZ: South Armorica Shear Zone; CCSZ:Coimbra-Cordoba Shear Zone). The age of ~ 320 Ma for shear zones in Corsica is from Giacomini *et al.* (2008).

Table 1. Analyzed samples.

Table 2 (ELA)-ICP-MS operating conditions.

Appendix 1 – Analytical Methods.

Appendix 2. (ELA)-ICP-MS isotopic data and calculated ages for zircons.

Time resolved signals were carefully inspected to detect common Pb and perturbations related to inclusions or fractures in zircon crystal that were excluded from integration intervals. Errors associated to the external standard reproducibility were propagated to each analysis according to Horstwood *et al.* (2003).

Appendix 3. (ELA)-ICP-MS isotopic results and calculated ages for monazites.

Analyses were carried out in the different domains revealed by BSE images. In order to have the most robust as possible results only data giving U-Pb concordant ages were considered. The presence of common Pb in monazite was monitored with the ^{204}Pb signal. However, the relatively high background prevents to detect small amounts of common Pb that may significantly alter the $^{207}Pb/^{235}U$ ratio. For this reason data interpretation was based on the $^{208}Pb/^{232}Th$ and $^{206}Pb/^{238}U$ ratios. All errors are reported in the text at 2σ level.

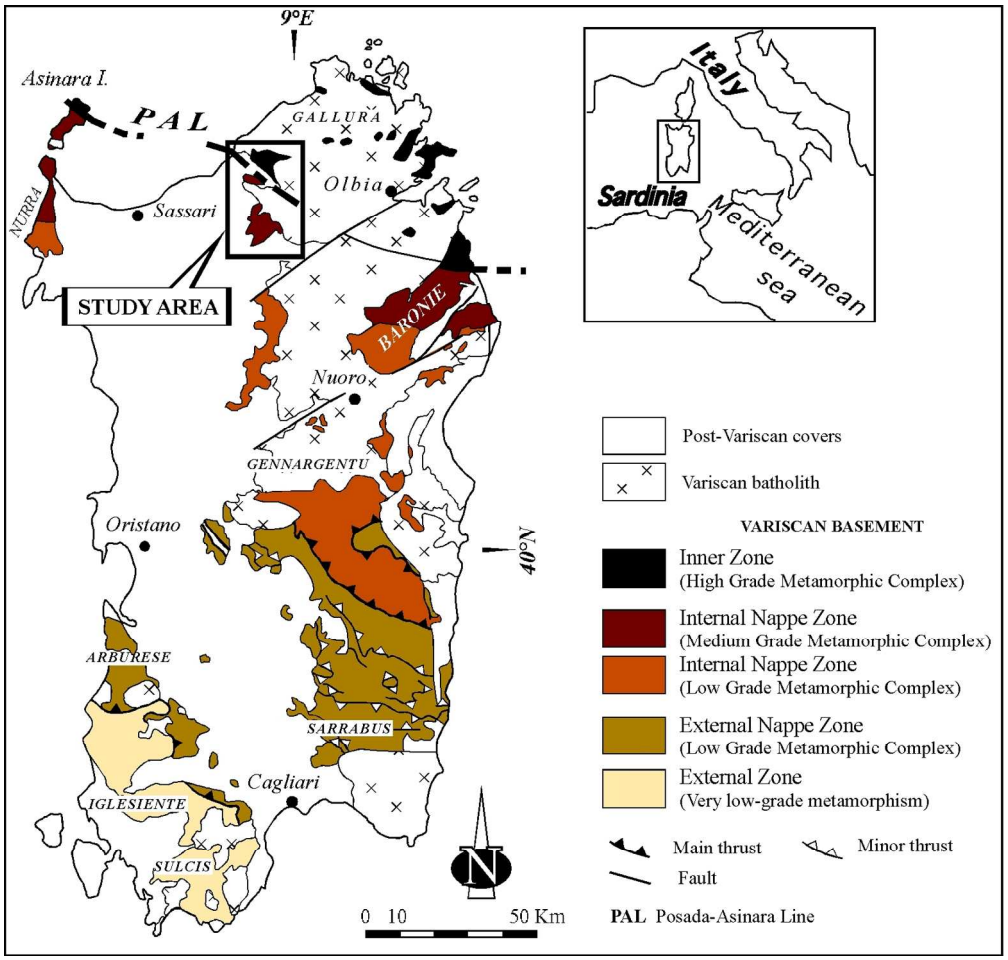

Fig. 1 Carosi et al.

Figure 1 color image
147x155mm (300 x 300 DPI)

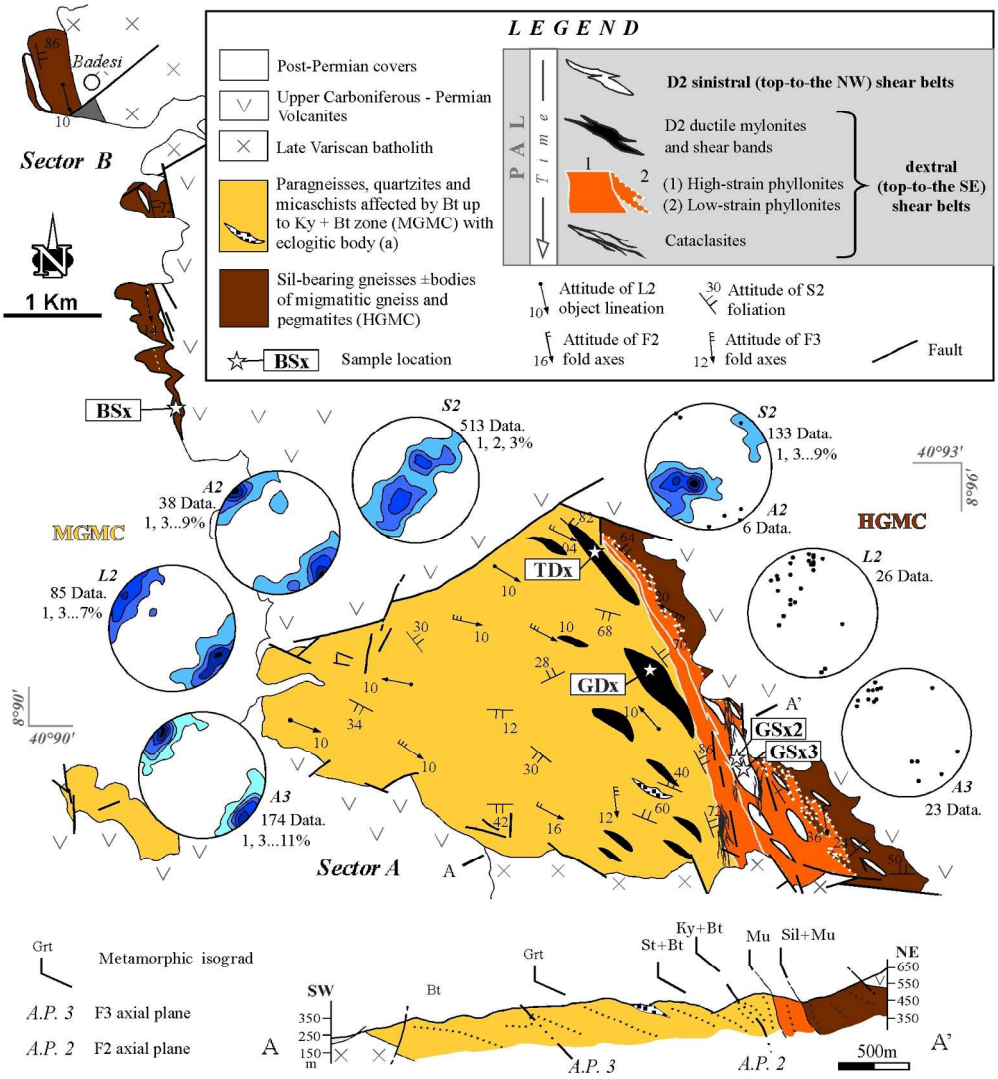

Fig. 2
Carosi et al.

Fig 2 color image, redrwan
165x194mm (300 x 300 DPI)

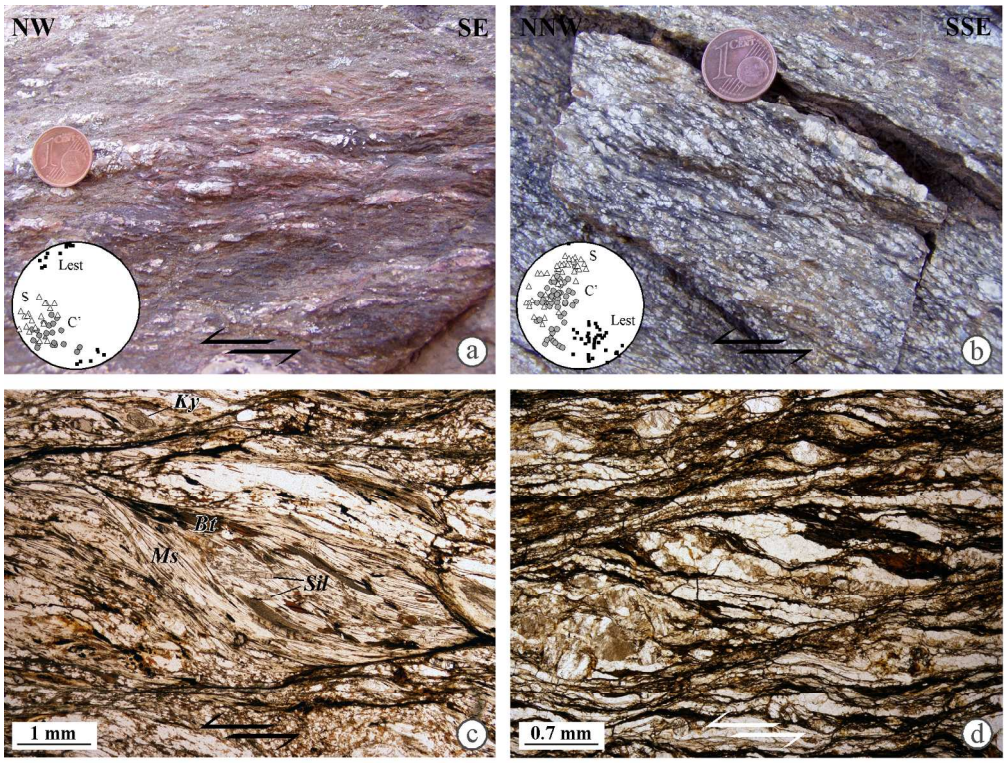

Fig. 3
Carosi et al.

Fig. 3
166x146mm (300 x 300 DPI)

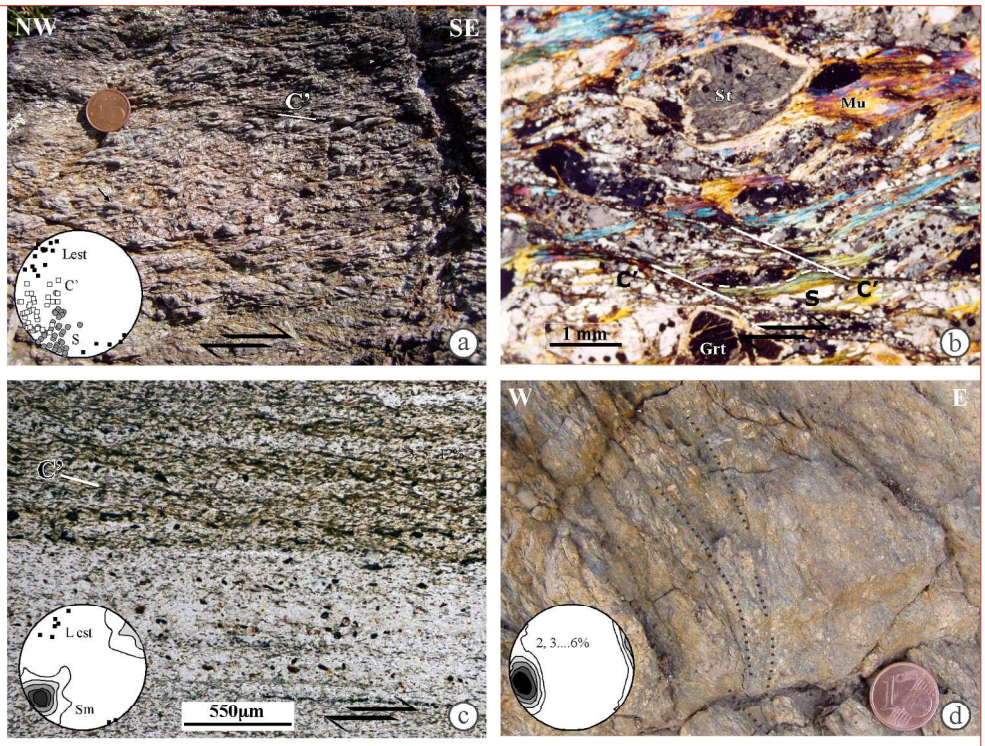

Fig. 4
Carosi et al.

Fig. 4
166x200mm (300 x 300 DPI)

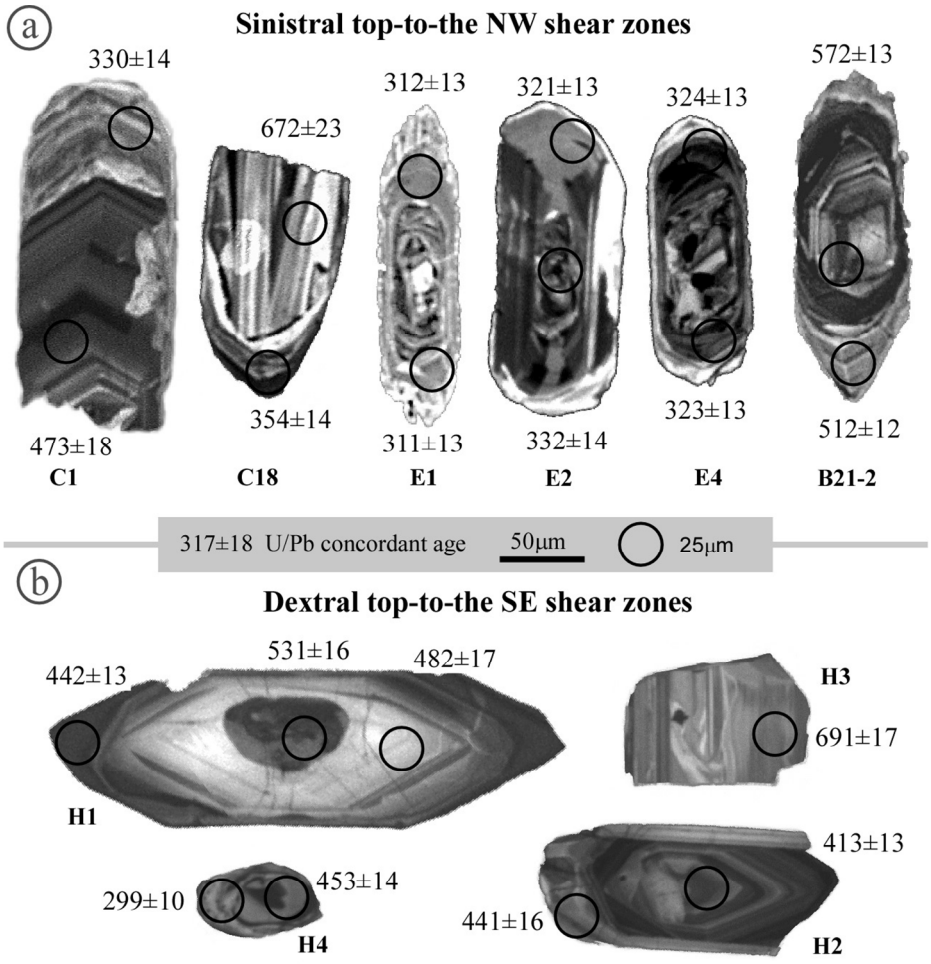

Fig. 5
Carosi et al.

Fig. 5
108x140mm (300 x 300 DPI)

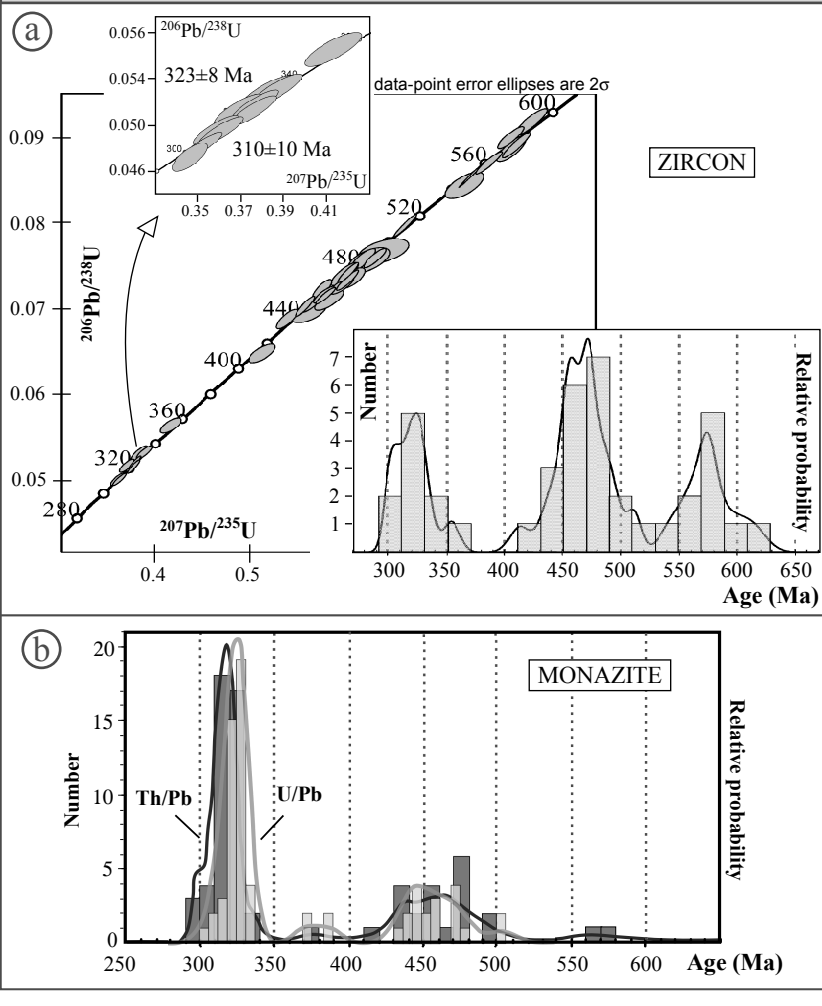

Fig. 6
Carosi et al.

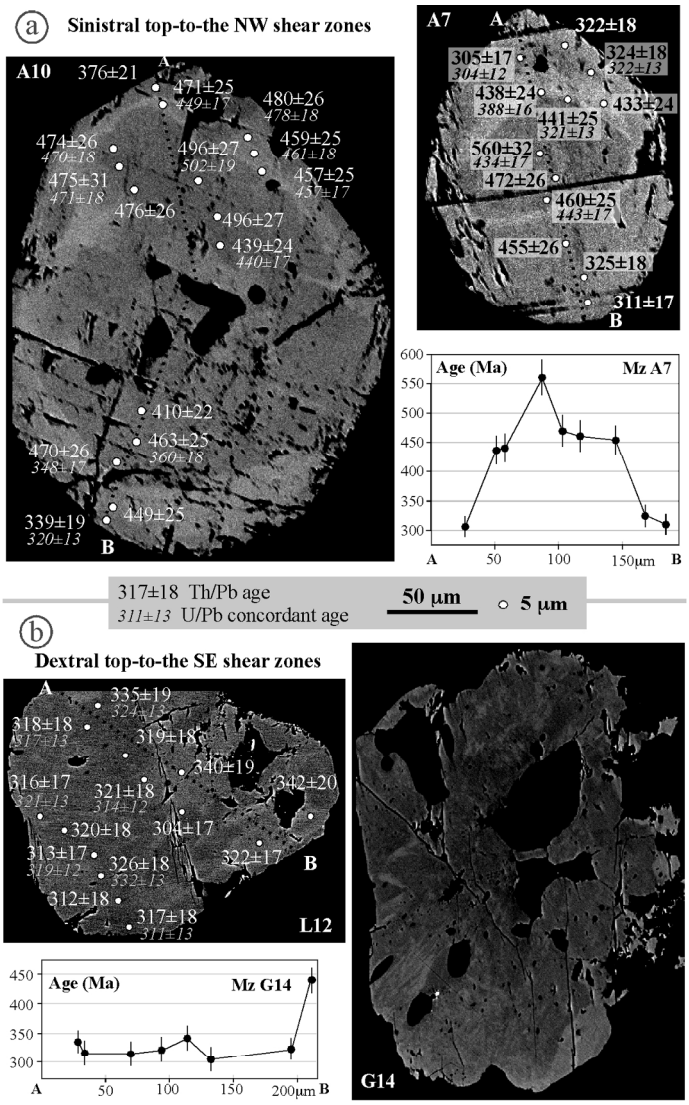

Fig. 7
Carosi et al.

Fig. 7
108x190mm (300 x 300 DPI)

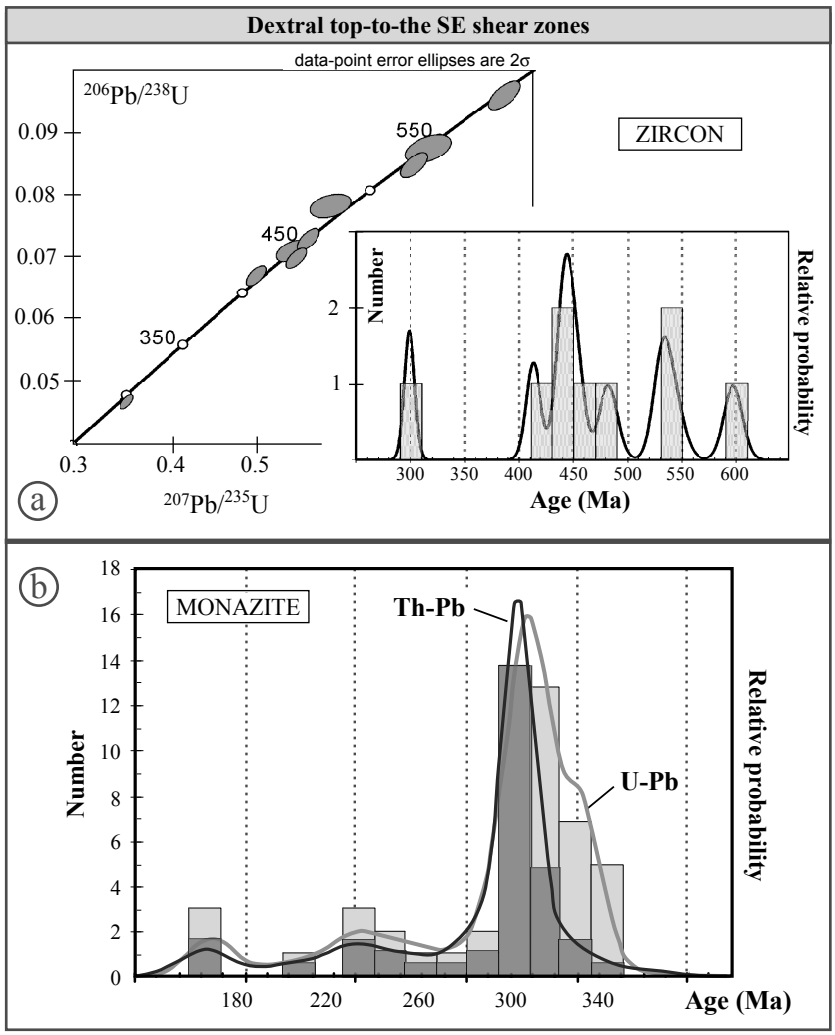

Fig. 8
Carosi et al.

Fig. 9

Fig. 9
138x232mm (300 x 300 DPI)

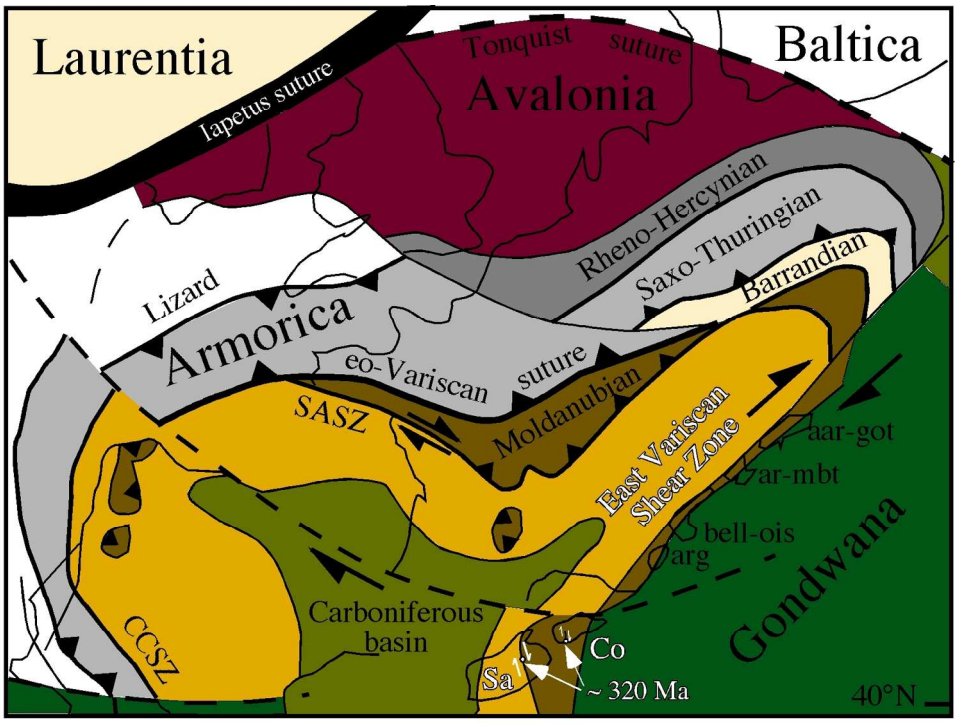

Fig.10 Carosi et al.

Fig. 10 new figure, color image
161x151mm (300 x 300 DPI)

Sample	Shear belt	Tectonic unit	Rock type	Mineral assemblage	Kinematic indicators	S plane	C-C' plane	Monazite	Zircon
TDx GDx	Dextral top-to-the SE	MGMC	Mylonitic micaschist	Grt, Bt, Pl, K-feld, St, Ky, Ms, Rt, Chl, Qtz	S-C/C' fabric, foliation fish, σ/δ porphyroclasts, Ms-/Bt-fish	Ms and Bt layers that enveloped kyanite, staurolite, garnet plagioclase crystals	Fine layers of insoluble material and thin and strongly recrystallized Qtz	Scarce, small and difficult to document in thin section	Small and elonged parallel to the mylonitic foliation
GSx2 GSx3	Sinistral top-to-the NW	HGMC	Mylonitic micaschist	Grt, Bt, Pl, K-feld, Ky, Sill, Ms, Rt, Chl, Qtz	S-C/C' fabric, σ/δ porphyroclasts, Ms-/Bt-fish	Layers of fine grained Ms and Bt crystals, and layers of Olig and plastically deformed Qtz ribbons	Oxides and locally small Qtz grains strongly interested by sub-grain rotation recrystallization	Difficult to document in thin section	Small and elonged parallel to the mylonitic foliation
BSx	Sinistral top-to-the NW	HGMC	Fine-grained mylonitic gneiss	Bt, Pl, K-feld, Ms, Rt, Chl, Qtz	S-C/C' fabric, σ/δ porphyroclasts, Ms-/Bt-fish				

Table 1- Samples description

Table 2 (ELA)-ICP-MS operating conditions

Inductively coupled plasma mass spectrometry (ICP-MS)	
Model	Element I, ThermoFinnigan
Mype	single collector double focusing magnetic sector ICP-MS
RF power	1100W
Gas flow:	*cooling* 13.5 l/min
	auxiliary 1.5 l/min
	carrier I (Ar) 1.0 l/min
	carrier II (He) 1.0 l/min
Acquired masses	^{202}Hg, ^{204}(Pb+Hg), ^{206}Pb, ^{207}Pb, ^{208}Pb, ^{232}Th, ^{238}U
Laser ablation	
Model	Geolas 200Q
Type	ArF excimer laser (Compex 102 from MicroLas)
Wave length	193 nm
Repetition rate	5 Hz(Zircon); 3 Hz (Monazite)
Fluency	12 J/cm^{-2}
Spot diameter	25 μm (Zircon); 10 μm (Monazite)
Procedure	
Zircon	Tiepolo (2003);Giacomini *et al.* (2006)
Monazite	Gasquet et al. (2010).
Standard	
Zircon	zircon 91500, 1064 Ma (Widenbeck *et al.* 1995)
Monazite	Moacir monazite (Seydoux-Guillaume et al., 2002)
Software	
Data reduction	GLITTER (van Achtenberg *et al.* 2001).
Concordant ages	Isoplot (Ludwig 2003)

Appendix 1

In-situ U-Pb geochronology of zircon and monazite was carried out with an excimer laser ablation (ELA)-ICPMS at C.N.R.-I.G.G.-U.O.S. of Pavia. The laser ablation instrument consists an ArF excimer laser microprobe at 193 nm (Geolas200Q-Microlas) with a sector field high resolution ICPMS Element I from Thermo Finnigan. The analytical methods are basically those described in Tiepolo (2003) and Paquette & Tiepolo (2007). Instrumental and laser-induced U/Pb fractionations were corrected with the matrix-matched external standard approach using the 91500 zircon (Widenbeck et al., 1995) and the Moacir monazite (Seydoux-Guillaume et al., 2002; Gasquet et al., 2010). The same integration intervals and spot size were used on both the external standard and unknowns. The spot size was set to 20 μm for zircon and to 10 μm for monazite. Laser fluency is 12J/cm^2. Data reduction was carried out using the "Glitter" software package (van Achterbergh et al., 2001) setting at 1% the error of the external standard. During each analytical run the reproducibility on the standards was propagated to all determinations according to the equation in Horstwood et al. (2003). After this operation, analyses are considered accurate within quoted errors. Concordia ages were determined and Concordia plots were constructed using the Isoplot/EX 3.0 software (Ludwig, 2003). All errors in the text are given at 2σ level.

Appendix 2 (ELA)-ICP-MS U/Pb isotopic data and calculated ages from zircons.

Sample	Zircon	$^{206}Pb/^{238}U$ ratio	±1σ	$^{207}Pb/^{235}U$ ratio	±1σ	$^{206}Pb/^{238}U$ Age	±1σ	$^{207}Pb/^{235}U$ Age	±1σ	Concordia Age	±2σ
GSx2	C25r	0.0948	0.0020	0.7641	0.0177	584	12	576	13	575	20
GSx2	C24r	0.3085	0.0067	44.698	0.1083	1734	37	1725	42	1720	34
GSx2	C2c	0.0764	0.0017	0.5916	0.0152	475	10	472	12	473	19
GSx2	C3r	0.0782	0.0017	0.6096	0.0155	486	11	483	12	484	19
GSx2	C3c	0.0794	0.0018	0.6316	0.0219	493	11	497	17	493	21
GSx2	C4/1r	0.0722	0.0016	0.5509	0.0133	449	10	446	11	446	17
GSx2	C4/2c	0.1026	0.0022	0.8580	0.0221	630	14	629	16	629	24
GSx2	C5r	0.0782	0.0018	0.6169	0.0193	486	11	488	15	486	21
GSx2	C6r	0.0660	0.0014	0.5063	0.0137	412	9	416	11	413	17
GSx2	C7/1c	0.4583	0.0099	10.084	0.2390	2432	52	2443	58	2449	31
GSx2	C7/2c	0.1097	0.0024	0.9342	0.0239	671	15	670	17	670	25
GSx2	C8c	0.0963	0.0021	0.7836	0.0195	593	13	588	15	588	22
GSx2	C9r	0.4611	0.0097	10.038	0.2351	2445	51	2438	57	2435	33
GSx2	C9c	0.4732	0.0098	10.238	0.2348	2498	52	2457	56	2433	32
GSx2	C10/1c	0.0942	0.0020	0.7632	0.0182	580	12	576	14	576	21
GSx2	C10/2c	0.1175	0.0025	10.238	0.0246	716	15	716	17	716	25
GSx2	C11r	0.0880	0.0019	0.7146	0.0199	544	12	548	15	545	22
GSx2	C11m	0.1001	0.0022	0.8315	0.0210	615	13	615	16	615	23
GSx2	C11c	0.1039	0.0023	0.8726	0.0219	637	14	637	16	637	24
GSx2	C12Ac	0.0894	0.0019	0.7222	0.0174	552	12	552	13	552	21
GSx2	C13Ac	0.0976	0.0021	0.8095	0.0216	600	13	602	16	601	24
GSx2	C15r	0.1194	0.0025	10.757	0.0266	727	15	742	18	739	26
GSx2	C14c	0.0785	0.0016	0.6225	0.0150	487	10	491	12	490	18
GSx2	C17A	0.0737	0.0015	0.5707	0.0138	458	10	459	11	458	18
GSx2	C17B	0.0766	0.0016	0.5951	0.0142	476	10	474	11	475	18
GSx2	C20A	0.0705	0.0015	0.5321	0.0133	439	9	433	11	436	17
GSx2	C20B	0.0713	0.0016	0.5545	0.0166	444	10	448	13	445	18
GSx2	C22	0.1468	0.0031	13.845	0.0327	883	18	882	21	882	27
GSx2	C23r	0.1056	0.0023	0.8988	0.0227	647	14	651	16	649	24
GSx2	C1r	0.0529	0.0011	0.3812	0.0098	332	7	328	8	330	14
GSx2	C1c	0.0757	0.0016	0.5945	0.0144	470	10	474	11	473	18
GSx2	C18c	0.1097	0.0023	0.9370	0.0221	671	14	671	16	672	23
GSx2	C18r	0.0566	0.0012	0.4132	0.0109	355	8	351	9	354	14
GSx2	C23c	0.1268	0.0027	11.219	0.0272	769	16	764	19	761	26
GSx3	E1r1	0.0496	0.0011	0.3577	0.0089	312	7	311	8	311	13
GSx3	E1r2	0.0494	0.0011	0.3601	0.0087	311	7	312	8	312	13
GSx3	E2r	0.0513	0.0011	0.3682	0.0091	323	7	318	8	321	13
GSx3	E2c	0.0530	0.0011	0.3865	0.0097	333	7	332	8	332	14
GSx3	E4r1	0.0517	0.0011	0.3760	0.0090	325	7	324	8	324	13
GSx3	E4r2	0.0512	0.0011	0.3751	0.0090	322	7	323	8	323	13
GSx3	E6r	0.0481	0.0010	0.3507	0.0082	303	6	305	7	304	12
BSx	6/2c	0.076	0.001	0.6020	0.010	472	5	479	8	473	11
BSx	5/1c	0.1016	0.001	0.8500	0.018	624	8	625	14	624	15
BSx	5/2r	0.0759	0.001	0.5992	0.012	472	6	477	10	472	10
BSx	5/1r 2	0.075	0.001	0.5886	0.011	466	5	470	9	468	11
BSx	24r	0.0745	0.001	0.5686	0.010	463	6	457	8	462	10
BSx	24c	0.0727	0.001	0.5582	0.011	452	6	450	9	452	11
BSx	21/2c	0.0927	0.001	0.7636	0.014	571	7	576	11	572	13
BSx	21/2r	0.0828	0.001	0.6543	0.012	513	6	511	9	512	12
BSx	23r	0.0933	0.001	0.7689	0.014	575	7	579	11	576	13
BSx	23c	0.0909	0.001	0.7402	0.013	561	7	563	10	561	14
BSx	21r	0.0736	0.001	0.5727	0.010	458	5	460	8	458	10
BSx	21c	0.073	0.001	0.5758	0.012	454	6	462	10	455	10
TDx	I2	0.113	0.0023	0.9749	0.0296	690	14	691	21	690	24
TDx	I5	0.0961	0.0019	0.7971	0.0157	591	12	595	12	597	17
TDx	I4c	0.1149	0.0022	0.9925	0.0126	701	13	700	9	699	9
TDx	I6c	0.1703	0.0033	17.175	0.0287	101	19	1015	17	1016	21
GDx	H5c	0.0875	0.0019	0.7055	0.0227	541	11	542	17	541	20
GDx	H4r	0.0468	0.0009	0.3452	0.0067	295	6	301	6	299	9.7
GDx	H4c	0.0728	0.0014	0.562	0.0109	453	9	453	9	453	14
GDx	H2c	0.0669	0.0013	0.4994	0.0095	418	8	411	8	413	13
GDx	H2r	0.071	0.0014	0.5421	0.0142	442	9	440	12	441	16
GDx	H1c	0.0698	0.0014	0.548	0.0101	435	8	444	8	442	13
GDx	H1c	0.0849	0.0017	0.6886	0.0132	525	10	532	10	531	16
GDx	H1m	0.0783	0.0016	0.5889	0.0202	486	10	470	16	482	17
GDx	H3r	0.1122	0.0022	0.9738	0.0165	685	13	690	12	691	17

(c = core; r = rim; m = intermediate portion)

Appendix 3 (ELA)-ICP-MS isotopic results and calculated ages for monazites

		$^{207}Pb/^{235}U$		$^{206}Pb/^{238}U$		$^{208}Pb/^{232}Th$		$^{206}Pb/^{238}U$		$^{207}Pb/^{235}U$		$^{208}Pb/^{232}Th$		U/Pb		
Sample	Mnz	ratio	±1σ	ratio	rsd	ratio	rsd	Age	2σ	Age	2σ	Age	2σ	Concordia age		2σ
TDx	L12-1	0.3468	0.00955	0.0495	0.0010	0.0158	0.0004	311.7	13.0	302.3	33.3	316.7	18.0	311		13
TDx	L12-2	0.3108	0.00895	0.0505	0.0011	0.0156	0.0004	317.3	13.5	274.8	31.7	312.3	18.0		discordant	
TDx	L12-3	0.3729	0.0103	0.0530	0.0011	0.0163	0.0005	332.6	13.7	321.8	35.6	326.4	18.4	332		13
TDx	L12-4	0.3292	0.00895	0.0509	0.0010	0.0156	0.0004	319.9	12.9	289.0	31.5	313.1	17.3		discordant	
TDx	L12-5	0.3345	0.0091	0.0501	0.0010	0.0160	0.0004	314.9	12.7	293.0	31.9	321.4	17.8	314		12
TDx	L12-6	0.3281	0.00895	0.0516	0.0010	0.0160	0.0004	324.6	13.1	288.1	31.4	319.8	17.7		discordant	
TDx	L12-7	0.3706	0.0103	0.0504	0.0010	0.0159	0.0005	317.2	13.2	320.1	35.5	318.6	18.1	317		13
TDx	L12-8	0.3676	0.0102	0.0517	0.0011	0.0167	0.0005	324.6	13.5	317.8	35.3	335.4	19.0	324		13
TDx	L12-9	0.3388	0.0092	0.0508	0.0010	0.0161	0.0004	319.6	12.7	296.3	32.1	322.2	17.7	319		12
TDx	L12-10	0.3157	0.0092	0.0551	0.0012	0.0152	0.0004	346.0	14.8	278.6	32.5	304.3	17.5		discordant	
TDx	L12-11	0.3187	0.00905	0.0543	0.0011	0.0170	0.0005	340.9	14.4	280.9	31.9	340.3	19.4		discordant	
TDx	L12-12	0.6273	0.01715	0.0542	0.0011	0.0171	0.0005	340.1	13.7	494.4	54.1	342.7	18.9		discordant	
TDx	L12-13	0.3487	0.00975	0.0512	0.0010	0.0158	0.0004	321.6	12.9	303.8	34.0	315.9	17.4	321		13
TDx	L12-14	0.3234	0.009	0.0515	0.0011	0.0160	0.0004	323.5	13.5	284.5	31.7	319.8	17.9		discordant	
TDx	L13a	0.3528	0.0043	0.0523	0.0009	0.0162	0.0002	328.3	11.7	306.8	14.9	324.0	7.6		discordant	
TDx	L13b	0.3673	0.0046	0.0514	0.0009	0.0160	0.0002	323.1	11.8	317.7	15.9	320.2	7.9	322		11
TDx	L13c	0.3513	0.00425	0.0516	0.0009	0.0161	0.0002	324.1	11.5	305.7	14.8	322.2	7.6		discordant	
TDx	L13d	0.3474	0.0042	0.0519	0.0009	0.0162	0.0002	326.2	11.6	302.8	14.7	325.0	7.6		discordant	
TDx	L11a	0.3476	0.0042	0.0508	0.0009	0.0160	0.0002	319.6	11.3	302.9	14.7	321.6	7.6		discordant	
TDx	L11b	0.3665	0.00445	0.0552	0.0010	0.0160	0.0002	346.6	12.3	317.1	15.4	320.0	7.6		discordant	
TDx	L11c	0.3683	0.00445	0.0551	0.0010	0.0159	0.0002	345.7	12.2	318.4	15.5	318.0	7.6		discordant	
TDx	L6a	0.4077	0.00495	0.0551	0.0010	0.0159	0.0002	346.0	12.3	347.2	16.9	317.9	7.6	346		12
TDx	L6b	0.3646	0.00445	0.0513	0.0009	0.0159	0.0002	322.3	11.7	315.7	15.7	318.2	7.9	321		11
TDx	L6c	0.3667	0.00445	0.0525	0.0009	0.0163	0.0002	329.9	11.7	317.2	15.4	326.0	7.6		discordant	
TDx	L6d	0.3595	0.0044	0.0544	0.0010	0.0160	0.0002	341.5	12.1	311.8	15.2	321.2	7.6		discordant	
TDx	L9a	0.3724	0.0045	0.0543	0.0010	0.0163	0.0002	340.7	12.0	321.4	15.6	326.6	7.6		discordant	
TDx	L9b	0.3628	0.0045	0.0544	0.0010	0.0159	0.0002	341.7	12.4	314.3	15.5	319.0	7.9		discordant	
TDx	L9c	0.3735	0.00445	0.0522	0.0009	0.0160	0.0002	328.0	11.5	322.2	15.8	321.4	7.6	327		11
TDx	L9d	0.4306	0.0053	0.0534	0.0009	0.0164	0.0002	335.4	11.8	363.6	17.9	329.6	7.6		discordant	
GDx	G14-a	0.3330	0.005	0.0490	0.0010	0.0134	0.0007	270.0	27.0	291.9	17.5	269.8	26.7		discordant	
GDx	G14-b	0.3370	0.005	0.0530	0.0010	0.0103	0.0005	208.0	18.0	294.9	17.5	207.7	18.4		discordant	
GDx	G14-c	0.3400	0.005	0.0520	0.0010	0.0159	0.0006	318.0	25.0	297.2	17.5	318.4	24.9		discordant	
GDx	G14-d	0.3410	0.005	0.0530	0.0010	0.0106	0.0004	212.0	18.0	297.9	17.5	212.1	17.8		discordant	
GDx	G14-e	0.3480	0.005	0.0540	0.0010	0.0158	0.0005	316.0	20.0	303.2	17.4	316.1	19.8		discordant	
GDx	G14-f	0.3410	0.005	0.0510	0.0010	0.0149	0.0005	298.0	19.0	297.9	17.5	297.9	19.0		discordant	
GDx	G14-g	0.3380	0.005	0.0510	0.0010	0.0129	0.0005	258.0	20.0	295.7	17.5	258.1	19.5		discordant	
GDx	G14-h	0.3480	0.005	0.0520	0.0010	0.0130	0.0005	260.0	18.0	303.2	17.4	260.3	18.3		discordant	
GDx	G14-i	0.3400	0.005	0.0540	0.0010	0.0103	0.0004	207.0	16.0	297.2	17.5	207.3	16.3		discordant	
GDx	G14-l	0.3440	0.005	0.0510	0.0010	0.0130	0.0004	260.0	18.0	300.2	17.5	260.1	17.6		discordant	
GDx	G14-m	0.3490	0.005	0.0520	0.0010	0.0140	0.0005	281.0	20.0	304.0	17.4	281.4	20.1		discordant	
GDx	G14-n	0.3260	0.0045	0.0510	0.0010	0.0174	0.0007	348.0	29.0	286.5	15.8	347.9	29.0		discordant	

GDx	G14-o	0.3420	0.005	0.0540	0.0010	0.0118	0.0004	238.0	17.0	298.7	17.5	237.5	16.7		discordant	
GDx	G14-p	0.3360	0.0045	0.0520	0.0010	0.0152	0.0005	305.0	18.0	294.1	15.8	304.9	18.1		discordant	
GDx	G14-q	0.3330	0.0045	0.0510	0.0010	0.0138	0.0005	278.0	19.0	291.9	15.8	277.8	19.4		discordant	
GDx	G1a	0.3600	0.0043	0.0523	0.0008	0.0158	0.0002	328.7	15.6	312.2	14.8	317.5	8.6		discordant	
GDx	G1b	0.3577	0.00425	0.0512	0.0008	0.0159	0.0002	321.8	15.3	310.5	14.7	318.2	8.6		discordant	
GDx	G1c	0.3614	0.0043	0.0509	0.0007	0.0163	0.0002	320.3	15.2	313.3	14.9	326.4	8.7	320		9
GDx	G1d	0.3505	0.00415	0.0507	0.0007	0.0158	0.0002	318.7	15.1	305.1	14.5	317.3	8.6		discordant	
GDx	G4a	0.3613	0.0043	0.0514	0.0008	0.0159	0.0002	323.4	15.4	313.2	14.9	319.4	8.6		discordant	
GDx	G4b	0.3482	0.00415	0.0512	0.0008	0.0161	0.0002	322.1	15.3	303.4	14.4	323.0	8.6		discordant	
GDx	G4c	0.4604	0.0055	0.0536	0.0008	0.0157	0.0002	336.8	16.1	384.5	18.3	315.5	8.2		discordant	
GDx	G4d	0.3856	0.0047	0.0522	0.0008	0.0164	0.0002	327.8	15.9	331.1	16.1	329.4	8.7	328		9
GSx2	F4a	0.3558	0.00435	0.0497	0.0009	0.0149	0.0002	312.4	11.0	309.1	15.2	299.1	6.8	312		11
GSx2	F4b	0.3551	0.0043	0.0527	0.0009	0.0158	0.0002	331.0	11.7	308.5	14.9	316.7	7.2		discordant	
GSx2	F4c	0.3543	0.0043	0.0528	0.0009	0.0156	0.0002	331.7	11.8	308.0	14.9	313.7	7.2		discordant	
GSx2	F4d	0.4247	0.00525	0.0526	0.0009	0.0168	0.0002	330.4	11.8	359.4	17.7	337.5	8.0		discordant	
GSx2	F16a	0.4210	0.00515	0.0522	0.0009	0.0161	0.0002	328.1	11.7	356.7	17.5	322.0	7.6		discordant	
GSx2	F16b	0.3624	0.0045	0.0511	0.0009	0.0161	0.0002	321.5	11.5	314.0	15.6	322.8	7.6	320		11
GSx2	F16c	0.3786	0.00535	0.0519	0.0010	0.0148	0.0002	326.4	12.3	326.0	18.5	296.9	7.8	326		12
GSx2	F16d	0.3885	0.00475	0.0520	0.0009	0.0159	0.0002	326.6	11.6	333.3	16.2	319.0	7.6	328		11
GSx2	F7a	0.3895	0.00475	0.0531	0.0009	0.0158	0.0002	333.5	11.9	334.0	16.3	317.7	7.6	334		11
GSx2	F7b	0.3795	0.00465	0.0523	0.0009	0.0161	0.0002	328.4	11.7	326.7	16.0	322.0	7.6	328		11
GSx2	F7c	0.3881	0.00475	0.0526	0.0009	0.0161	0.0002	330.6	11.8	333.0	16.2	323.2	7.6	331		11
GSx2	F7d	0.3652	0.0045	0.0515	0.0009	0.0159	0.0002	323.6	11.5	316.1	15.5	319.4	7.2	322		11
GSx2	F2a	0.3764	0.0046	0.0510	0.0009	0.0158	0.0002	320.8	11.3	324.3	15.8	315.9	7.2	321		11
GSx2	F2b	0.3682	0.00465	0.0513	0.0009	0.0160	0.0002	322.6	11.7	318.3	16.1	321.0	7.9	322		11
GSx2	F2c	0.3865	0.00485	0.0533	0.0010	0.0161	0.0002	334.4	12.2	331.8	16.6	321.8	7.9	334		12
BSx	A7-1	0.3499	0.0099	0.0509	0.0011	0.0169	0.0005	320.3	13.3	304.6	34.6	338.7	19.3	320		13
BSx	A7-2	0.3994	0.01105	0.0724	0.0014	0.0225	0.0006	450.7	18.0	341.2	37.7	449.5	24.7		discordant	
BSx	A7-3	0.5634	0.0155	0.0719	0.0014	0.0235	0.0006	447.5	18.0	453.7	50.0	470.3	25.8	448		17
BSx	A7-4	0.5577	0.0152	0.0741	0.0015	0.0232	0.0006	460.9	18.2	450.1	49.0	462.6	25.1	460		18
BSx	A7-5	12.716	0.0347	0.0705	0.0014	0.0205	0.0006	438.9	17.4	833.1	90.9	410.2	22.1		discordant	
BSx	A7-6	0.4991	0.01375	0.0710	0.0014	0.0220	0.0006	442.1	17.3	411.1	45.3	439.3	23.6	440		17
BSx	A7-7	0.5504	0.01515	0.0816	0.0016	0.0249	0.0007	505.4	20.0	445.3	48.9	496.5	27.0		Discordant	
BSx	A7-8	0.7072	0.0193	0.0809	0.0016	0.0249	0.0007	501.5	19.6	543.1	59.4	496.1	26.7	502		19
BSx	A7-9	0.5619	0.01565	0.0735	0.0015	0.0229	0.0006	457.4	18.1	452.8	50.4	457.2	24.7	457		17
BSx	A7-10	0.5671	0.0157	0.0742	0.0015	0.0230	0.0006	461.6	18.3	456.2	50.5	458.8	24.8	461		18
BSx	A7-11	0.6089	0.01645	0.0769	0.0015	0.0240	0.0007	477.6	18.7	482.8	52.2	479.6	26.1	478		18
BSx	A7-12	0.5160	0.014	0.0761	0.0015	0.0238	0.0006	472.7	18.5	422.4	45.8	475.8	25.7		discordant	
BSx	A7-13	0.5856	0.0159	0.0758	0.0015	0.0288	0.0008	470.9	18.4	468.1	50.8	574.7	31.0	471		18
BSx	A7-14	0.5560	0.0154	0.0758	0.0015	0.0237	0.0007	470.8	19.0	448.9	49.7	474.0	26.2	470		18
BSx	A7-15	0.5529	0.0152	0.0722	0.0014	0.0236	0.0006	449.3	17.8	446.9	49.1	471.3	25.5	449		17
BSx	A7-16	0.5033	0.01365	0.0593	0.0012	0.0188	0.0005	371.5	14.8	414.0	44.9	376.5	20.6		discordant	
BSx	A10-1	0.4166	0.0113	0.0507	0.0010	0.0155	0.0004	318.6	13.0	353.6	38.4	310.9	17.5		discordant	
BSx	A10-2	0.3192	0.00875	0.0502	0.0010	0.0162	0.0004	315.8	12.6	281.2	30.8	324.8	17.8		discordant	
BSx	A10-3	0.4067	0.01165	0.0719	0.0015	0.0228	0.0006	447.3	18.6	346.5	39.7	455.1	25.7		discordant	

BSx	A10-4	0.5375	0.0147	0.0711	0.0014	0.0230	0.0006	443.0	17.8	436.8	47.7	459.6	25.4	443		17
BSx	A10-5	0.5358	0.0146	0.0759	0.0015	0.0236	0.0006	471.8	18.9	435.6	47.4	472.1	25.9		discordant	
BSx	A10-6	0.4980	0.01375	0.0699	0.0014	0.0281	0.0008	435.3	17.9	410.3	45.3	560.5	31.4	434		17
BSx	A10-7	0.4753	0.0135	0.0621	0.0013	0.0219	0.0006	388.3	16.1	394.8	44.9	437.7	24.4	388		16
BSx	A10-8	0.3300	0.00905	0.0483	0.0010	0.0152	0.0004	304.1	12.4	289.6	31.7	304.7	17.1	304		12
BSx	A10-9	0.3167	0.00865	0.0522	0.0011	0.0161	0.0004	328.3	13.4	279.3	30.5	321.8	18.0		discordant	
BSx	A10-10	0.3819	0.0105	0.0511	0.0011	0.0162	0.0005	321.5	13.4	328.4	36.1	324.0	18.3	322		13
BSx	A10-11	0.3874	0.0108	0.0596	0.0012	0.0217	0.0006	372.9	15.2	332.4	37.1	433.9	24.0		discordant	
BSx	A10-12	0.4716	0.01305	0.0622	0.0013	0.0221	0.0006	389.0	15.9	392.3	43.5	441.6	24.6	389		15
BSx	A6a	0.3655	0.0043	0.0520	0.0007	0.0160	0.0002	326.7	15.4	316.3	14.9	320.2	8.9		discordant	
BSx	A6b	0.3609	0.00425	0.0527	0.0008	0.0162	0.0002	331.0	15.6	312.9	14.7	324.6	9.0		discordant	
BSx	A6c	0.3620	0.0043	0.0518	0.0007	0.0159	0.0002	325.8	15.4	313.7	14.8	318.0	8.6		discordant	
BSx	A6d	0.3557	0.0042	0.0513	0.0007	0.0159	0.0002	322.5	15.2	309.0	14.6	318.8	8.6		discordant	
BSx	A9a	0.3910	0.00465	0.0528	0.0008	0.0157	0.0002	331.4	15.7	335.1	15.9	314.5	8.5	332		9
BSx	A9b	0.3582	0.00425	0.0520	0.0007	0.0160	0.0002	326.9	15.5	310.9	14.8	320.8	8.6		discordant	
BSx	A9c	0.3821	0.00455	0.0516	0.0007	0.0157	0.0002	324.2	15.4	328.6	15.6	315.1	8.6	324		9
BSx	A9d	0.3640	0.0044	0.0515	0.0008	0.0151	0.0002	323.6	15.6	315.2	15.2	302.9	8.4	323		9
BSx	A14a	0.3484	0.0042	0.0494	0.0007	0.0149	0.0002	311.0	15.0	303.5	14.6	298.3	8.1	310		9
BSx	A14b	0.3848	0.00455	0.0525	0.0008	0.0162	0.0002	329.7	15.6	330.5	15.7	325.2	8.3	330		9
BSx	A14c	0.5432	0.0070	0.0711	0.0011	0.0219	0.0003	442.9	22.8	440.5	22.7	437.3	12.3	443		13
BSx	A14d	0.4665	0.0059	0.0508	0.0008	0.0163	0.0002	319.2	16.2	388.7	19.7	325.8	9.0		discordant	